

Laboratory experiments on three-dimensional deformable granular landslides on planar and conical slopes

Abstract Landslides of subaerial and submarine origin may generate tsunamis with locally extreme amplitudes and runup. While the landslides themselves are dangerous, the hazards are compounded by the generation of tsunamis along coastlines, in enclosed water bodies, and off continental shelves and islands. Tsunamis generated by three-dimensional deformable granular landslides were studied on planar and conical hill slopes in the three-dimensional NEES tsunami wave basin at Oregon State University based on the generalized Froude similarity. A unique pneumatic landslide tsunami generator (LTG) was deployed to control the kinematics and acceleration of the naturally rounded river gravel and cobble landslides to simulate broad ranges of landslide shapes and velocities along the slope. Lateral and overhead cameras are used to measure the landslide shapes and kinematics, while acoustic transducers provide the shape of the subaqueous deposits. The subaerial landslide shape is extracted from the camera images as the landslide propagates under gravity down the hill slope, and surface reconstruction of the landslide is conducted using the stereo particle image velocimetry (PIV) system on the conical hill slope. Subaerial landslide surface velocities are measured with a planar PIV system on the planar hill slope and stereo PIV system on the conical hill slope. The submarine deposits are characterized by the runout distances and the deposit thickness distributions. Larger cobbles are observed producing hummock type features near the maximum runout length. These unique laboratory landslide experiments serve to validate deformable landslide models as well as provide the source characteristics for tsunami generation.

Keywords Granular landslides · Physical modeling · Landslide tsunami generator · Particle image velocimetry · Three-dimensional experiments · Image processing

Introduction

Massive landslides can convert into highly fluid, rapid debris avalanches attaining long runout distances that can be multiples of the vertical drop height. Long runout debris avalanches exhibit the most spectacular and complex high-speed motion. The unpredictability associated with debris avalanche dynamics may pose threat to life and property, mainly in mountainous regions. Detailed sturzstrom characteristics were first observed at Elm (Switzerland) in 1881 (Heim 1882, 1932; Hsü 1975). The Elm landslide highlighted the transition from a slate quarry rockfall to a dry debris flow resulting in an up surge on the opposing mountain slope and a long runout down the nearly flat valley floor. The term sturzstrom was coined by the Elm event with an estimated maximum landslide velocity of $v_s = 80$ m/s and a landslide volume $V_s = 10 \times 10^6$ m³ (Heim 1932). The highest bulk landslide velocities of up to $v_s \leq 150$ m/s were estimated for the Huascarán debris avalanche in Peru with a vertical drop height of 4000 m (Körner 1983). On

May 31, 1970, a magnitude $M_w = 7.9$ earthquake located 20 km off the coast of Peru triggered thousands of landslides in the Cordillera Blanca and the Cordillera Negra (Plafker et al. 1971). Perhaps half of the total earthquake triggered landslide volume was contained in the single massive failure of the west flank of the north peak of Nevados Huascarán at elevations between 5400 and 6500 m, located some 130 km east of the epicenter. The resulting debris avalanche with a volume of $V_s = 100 \times 10^6$ m³ was composed of granite rock, ice, glacial sediments, and water (Plafker and Ericksen 1979). The 1970 Huascarán event buried the city of Yungay and 18,000 people below 30 m of debris resulting in the deadliest landslide of non-volcanic origin. Other well-documented cases include the Sherman Glacier rock avalanche (Alaska) in 1964 (Shreve 1966, 1968; McSaveney 1978), the 1991 Randa rockslides (Switzerland) (Sartori et al. 2003), and the prehistoric Blackhawk landslide (California) (Shreve 1968).

Particularly, hazardous are landslides into confined water bodies as well as at islands, along continental shelves and shorelines, where they may generate tsunamis traveling both in the offshore and along shore directions. The tsunami hazard extends beyond the immediate landslide path of movement. Landslide-generated tsunamis can be hazardous in the near field regions due to locally high amplitudes and runup. Characteristic tsunamis caused by landslides were recorded at Grand Banks in 1929 (Fine et al. 2005), Lituya Bay, Alaska in 1958 (Fritz et al. 2001, 2009; Weiss et al. 2009; Xenakis et al. 2017), Vajont dam in Italy in 1963 (Müller 1964), the 1998 Papua New Guinea event (Synolakis et al. 2002; Bardet et al. 2003), Stromboli volcano in 2002 (Tinti et al. 2005, 2006), the 2006 Java tsunami (Fritz et al. 2007), the 2010 Haiti earthquake (Fritz et al. 2013), and the ancient Storegga slides (Bondevik et al. 2005). The resulting tsunami waves can cause damage due to high local runup along the coastline and overtopping of dams and reservoirs. The field data from landslide generated tsunami events are mostly limited to slide scarps, submarine slide deposits, far field tide gauge recordings, and onshore wrack- and trimlines produced by the wave runup. The information on the landslide characteristics and kinematics, landslide water body coupling, wave generation, and the near field wave characteristics are often widely lacking or incomplete. Physical models of granular landslide generated tsunamis provide insight on the wave generation and propagation mechanisms (Fritz 2002a; Fritz et al. 2004; Zweifel et al. 2006; Ataie-Ashtiani and Najafi-Jilani 2008; Heller and Hagar 2010; Mohammed 2010; Mohammed and Fritz 2012, 2013; McFall 2014; McFall and Fritz 2016, 2017; Bregoli et al. 2017; Miller et al. 2017; Yavari-Ramshe and Ataie-Ashtiani 2017). These models further provide high precision data to advance numerical modeling efforts of tsunami generation by landslides. The experimental results on subaerial landslide motion along planar and conical slopes are discussed in the following sections.

Experimental studies on granular landslides range from early one-dimensional studies of mass flow down rough inclines to unconfined three-dimensional mass flow over complex topographies. One-dimensional studies were conducted by Huber (1980), Plüss (1987), and Koch (1989), which were extended to include lateral granular spreading and fully three-dimensional granular landslides by Koch et al. (1994), Gray et al. (1999), Iverson et al. (2004), and Pudasani et al. (2008). Experiments with finite granular mass on straight inclined chutes with a curved transition to horizontal were conducted by Savage and Hutter (1991) and Hutter et al. (1995), in exponential curved chutes by Hutter and Koch (1991) and in a curved chute with a bump to allow for mass separation by Greve and Hutter (1993). These experimental results were used for validation of the Savage-Hutter avalanche models (Savage and Hutter 1989, 1991). Comparative studies were made by Hutter and Koch (1991), Gray et al. (1999), Tai et al. (1999, 2001), Wieland et al. (1999), and Pudasani et al. (2008) among others. In most of these experiments, the granular material constituting the landslide mass was released from rest, which resulted in an instant collapse of the landslide mass. In order to study landslide propagation in a higher range of kinematics, the initial position has to be moved upwards resulting in a decrease in landslide thickness with increasing velocity. In nature, many landslides originate as a sliding block which transitions from sliding block to a debris avalanche downslope or at slope changes (Varnes 1978). This study builds upon previous work with the introduction of a pneumatic landslide tsunami generator on a three-dimensional slope to provide various initial accelerations and release points to the landslide material in an attempt to mimic the transition from block sliding to debris avalanche in the laboratory. However, the pneumatic landslide tsunami generator experiments described in the subsequent sections are applicable to subaerial cases where the landslide material is composed of granular material. The presented pneumatic landslide tsunami generator has not been applied to cases where the landslide moves as a solid block from failure to impact with the water surface. An example is the event of a landslide generated tsunami in Vajont reservoir, Italy in 1963, where the landslide moves over a relatively short distance as a solid block without disintegrating (Müller 1964; Hendron and Patton 1985; Nonveiller 1987; Genevois and Ghirelli 2005; Crosta et al. 2016). The physical model does not represent cases where the landslides originate as partially submerged alluvial delta sediments such as in Haiti 2010 (Fritz et al. 2013) or submarine cohesive sediments such as in the ancient Storegga slide (Bondevik et al. 2005). The laboratory experiments neither include partially submerged or submarine landslide cases nor cases where the landslide material is composed of cohesive sediments, fine soils, and clays (Watts 2000; Locat 2001; Locat and Lee 2002; Urgeles et al. 2002; Enet and Grilli 2005, 2007; Grilli and Watts 2005; Poncet et al. 2010). The physical model is applicable to gravity driven subaerial landslides on hill slopes or volcanic flank collapses. The advanced measurements of landslide characteristics from this study can be used to validate deformable landslide models and improve numerical modeling efforts of landslide tsunami generation with improved source characteristics. This manuscript analyzes the landslide characteristics. The tsunami wave generation, offshore propagating wave characteristics, and lateral wave and offshore wave runup from this study are thoroughly analyzed and detailed in Mohammed and Fritz (2012, 2013) and McFall and Fritz (2016, 2017).

Physical model with pneumatic landslide generator

Planar and conical hill slopes in three-dimensional tsunami wave basin

The experiments on flow of three-dimensional deformable granular landslides and tsunami generation were conducted at the O. H. Hinsdale Wave Research Laboratory at the Oregon State University, Corvallis, Oregon in three phases. The first two phases generated landslides on a planar hill slope, and the third phase generated landslides on a conical hill slope, simulating a landslide off an island or a volcanic flank collapse. The physical models were setup in the three-dimensional NEES tsunami wave basin (TWB) measuring 48.8 m × 26.5 m × 2.1 m. Experiments were conducted at water depths $h = 0.3, 0.6, 0.9, 1.2,$ and 1.35 m. The planar hill slope model was built on one end of the wave basin with an inclination of $\alpha = 27.1^\circ$, as shown in Fig. 1a. The conical island model was built with a base diameter of 10 m and with the same angle as that of the planar hill slope model, $\alpha = 27.1^\circ$ (McFall and Fritz 2016, 2017).

The landslides were modeled with two different materials. Naturally rounded river gravel was used on the planar and conical hill slopes with $d_{50} = 13.7$ mm within a sieve size range of 12.7 to 19.1 mm (Fig. 1d). Naturally rounded river cobbles were used on the conical hill slope with a grain size diameter larger than the 19.1 mm sieve, and some cobbles were larger than 100 mm in all dimensions (Fig. 1e). Both materials were mined from the Willamette River, Oregon and had a grain density $\rho_g = 2.6$ t/m³, bulk slide density $\rho_s = 1.76$ t/m³, porosity $n = 0.31$, effective internal friction angle $\phi' = 41^\circ$, and basal friction angle on steel $\delta = 23^\circ$. The equivalent effective internal friction angle may be attributed to the matching porosity, indicating smaller granulates infilling voids around larger cobbles in the cobble landslide and the matching naturally rounded grain shape of the landslide materials (Li and Komar 1986; Buffington et al. 1992). Experiments were conducted with two landslide volumes V_s of 0.756 and 0.378 m³ corresponding to landslide masses m_s of 1350 and 675 kg.

Pneumatic setup

The landslides were simulated by a pneumatic landslide tsunami generator (LTG), which allowed controlling the acceleration and shape of the landslide on the hill slope. The design of the LTG mimics natural landslide motion on the hill slope, where some landslides initially move as a solid block, followed by disintegration under the influence of basal friction, internal friction, and gravity to collapse into a debris avalanche on a hill slope. The landslide material is loaded into an aluminum slide box (2.1 m × 1.2 m × 0.3 m) riding on ultra-high-molecular weight polyethylene (UHMWPE) plastic gliders with lateral rail guides and accelerated by four pneumatic drives as shown in Fig. 1b. The gliders ensure the slide box moves smoothly in the direction of the piston motion, without any additional friction. The standard double-acting stainless steel cylinders with rods had a piston diameter of 0.1 m and a stroke length of 2 m. The pneumatic scheme with the circuit for the box motion with separate branches for the forward and backward thrusts is shown in Fig. 1c. A two-stage stationary air compressor with an integrated 0.303 m³ air reservoir supplies the compressed air. An additional 0.303 m³ air reservoir connecting directly to the solenoid valves was necessary to preset ventilation pressure and avoid a significant pressure drop in the ventilation chambers of the pneumatic drives during the slide box

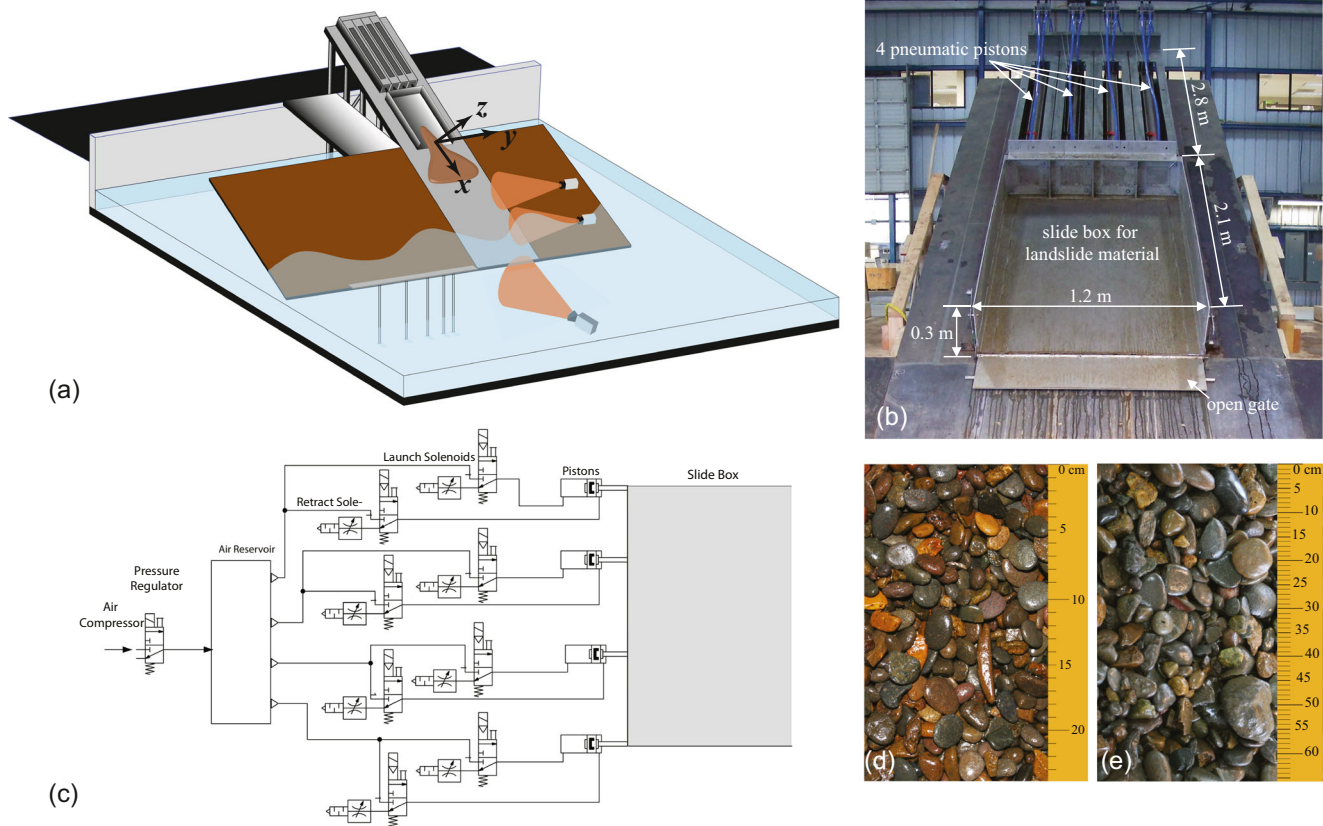


Fig. 1 a Pneumatic landslide tsunami generator (LTG) setup on a planar hill slope in the tsunami wave basin with an array of above water and underwater cameras. b LTG slide box in the retracted position with an open gate after a launch. c Pneumatic scheme with circuits driving the LTG box motion. d Naturally rounded river gravel and e river cobbles

acceleration. The pneumatic setup consisting of a circuit with the four pneumatic drives was tuned for maximum slide box acceleration and peak velocity. The dynamics of the piston motion primarily depend on the pressure difference between the two cylinder chambers and the duration of the pressure difference build-up (Ohmer 1994; Fritz and Moser 2003). Connecting a three-way solenoid valve directly with each cylinder end minimized the duration of the pressure difference build-up and allowed individual control.

Landslide generator operating principle

A precision proportional pressure regulator adjusts the reservoir air pressure p_r between 4 and 10 bar prior to the launch. The pneumatic system was controlled with preset trigger signals, while proximity switches served as safety. Prior to each experiment, the trigger settings were determined and programmed to the integrated controller. In the initial position before the start, the acceleration pressure $p_a = 0$ corresponds to the atmospheric pressure according to the pneumatic convention. The initial deceleration pressure $p_d = p_r$ was necessary to hold the loaded slide box in the starting position. After pressing the start button, a calibrated sequence of control signals were sent to the valves. First, the deceleration pressure p_d was reduced by switching to exhaust for a short pressure-dependent time avoiding premature gravitational slide box

motion. Subsequently, the slide box is launched by ventilation rapidly building up the acceleration pressure p_a . The initial acceleration was larger than gravity g allowing the flap initially containing the granular material in the slide box to open mechanically with the initiation of downhill box motion. The maximum box velocity v_b was reached approximately at half stroke, and the landslide material was released from the confined box motion into a purely gravity driven landslide. The valves at both cylinder ends were switched to decelerate the slide box pneumatically by the reversed pressure gradient $p_a < p_d$. Exhausting at the upper end of the cylinders reduced the driving force, while simultaneous ventilation at the lower end of the cylinders actively decelerated and ultimately retracted the slide box back into the starting position.

The LTG is placed on the hill slope such that the initial position of the front of the slide box can be varied along the ramp. The pneumatic LTG allowed varying the dynamic landslide parameters before impact providing various landslide source characteristics to investigate their effect on the tsunami generation. The parameters varied in the experiments are the initial slide box acceleration, the landslide release location along the ramp, the landslide volume, and the water depth. These settings controlled the variability of the dynamic landslide parameters at impact such as the landslide front velocity v_s , thickness s , and width b .

Landslide generator performance

The landslide motion is characterized by the coordinates (x_s, y_s, z_s) along the hill slope with the origin at the initial rest position of the slide box front. The coordinate x_s follows the hill slope and transitions to the TWB bottom at the toe of the hill slope. The y_s coordinate follows the hill slope width in the direction of the lateral slide spreading, and z_s is perpendicular to the slope. The slide is characterized by the measured thickness $s(x_s, y_s, t)$, width $b(x_s, y_s, t)$, and slide surface velocity $u_s(x_s, y_s, t)$. The initial slide thickness s_0 is considered as the length scale for non-dimensionalizing the parameters in the LTG framework. The velocity is non-dimensionalized by $v_0 = \sqrt{gs_0}$ and time by $t_0 = \sqrt{s_0/g}$. The non-dimensional parameters X, Y, Z, T, S, B , and U_s are related to the dimensional parameters by

$$[x_s, y_s, z_s] = s_0[X, Y, Z] \tag{1}$$

$$[s, b] = s_0[S, B] \tag{2}$$

$$[u_s] = \sqrt{gs_0}[U_s] \tag{3}$$

$$[t_s] = \sqrt{\frac{s_0}{g}}[T] \tag{4}$$

The slide front velocity is denoted as $v_s = v(x_f)$, where x_f is the location of the slide front. The corresponding non-

dimensional slide Froude number is denoted by $F_s = v_s/\sqrt{gs_0}$. The slides are launched at a slide box velocity v_b , and the corresponding non-dimensional slide box Froude number is $F_b = v_b/\sqrt{gs_0}$. The non-dimensional slide volume is denoted by $V = V_s/s_0^3$. The non-dimensional water depth normalized by the initial slide thickness s_0 is denoted by H . A total of 208 experimental trials were conducted with the gravel landslide on the planar hill slope, 90 trials with the gravel landslide on the conical hill slope, and 42 trials with the cobble landslide on the conical hill slope. This resulted in non-dimensional landslide parameters in the following ranges: landslide Froude number at impact, $2.2 < F_s < 3.8$, relative landslide thickness, $0.1 < S < 1$, relative landslide width, $4 < B < 11.8$, relative landslide volume, $14 < V < 28$, and relative water depth, $1 < H < 4$.

The motion of the pneumatic slide box was measured with four cable extension transducers on the four pneumatic piston rods. The potentiometric cable extension transducers have an operating accuracy of ± 0.25 to $\pm 0.1\%$ with a repeatability of $\pm 0.02\%$ over the full stroke. These transducers in combination with video cameras were used to obtain the displacement of the slide box and to derive slide box velocity and acceleration. The peak box Froude number varied in the range $1.2 \leq F_b \leq 2.4$, corresponding to peak box velocity $2.2 \text{ m/s} \leq v_b \leq 4.0 \text{ m/s}$ depending on the initial box acceleration and landslide volume. As the air flow is reversed, the slide material exits the box close to the peak velocity and collapses into a gravity driven landslide traveling downslope with unconfined lateral deformation. The slide box and landslide front velocity are shown in Fig. 2. The initial peak acceleration spike of the loaded slide box reached up to $4g$. However, the initial acceleration spikes were only recorded for a few milliseconds, and then acceleration rapidly

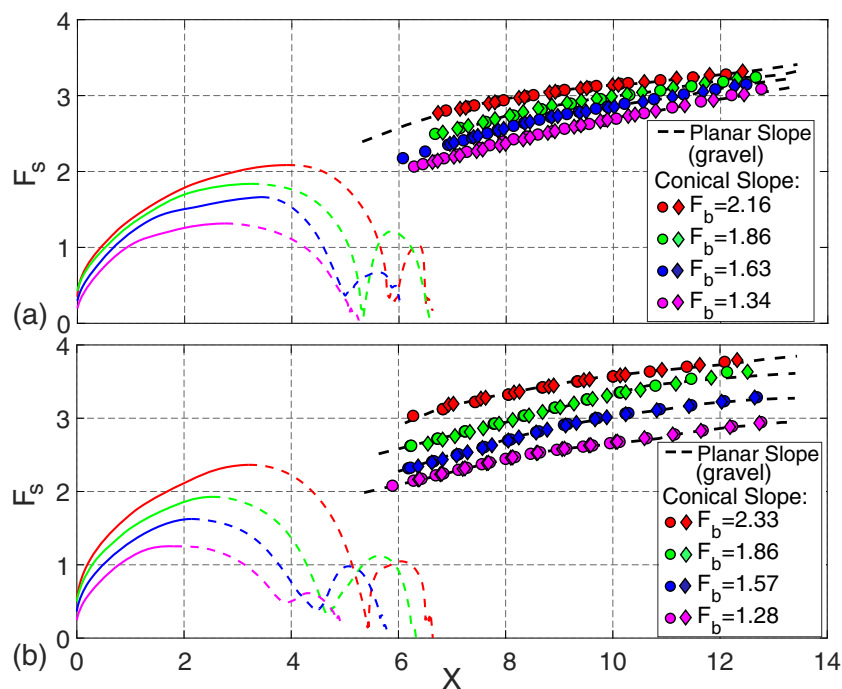


Fig. 2 Dimensionless velocity of the slide box (on left) and landslide front for both gravel (dashed line and circles) and cobble (diamonds) landslides as a function of the dimensionless propagation distance X on the planar and conical hill slopes with landslide volumes **a** $V = 28$ and **b** $V = 14$

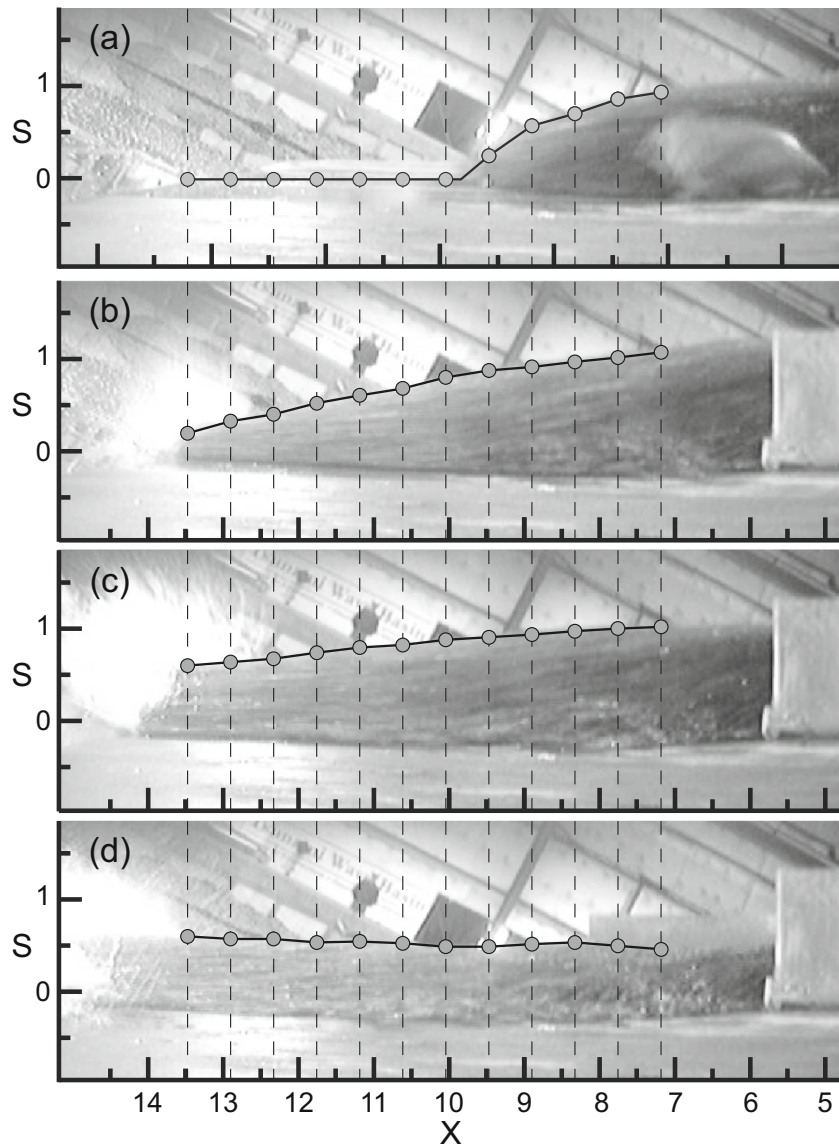


Fig. 3 Above water camera images with collected data points related to landslide thickness at **a** $T = 4.40$, **b** $T = 5.55$, **c** $T = 6.35$, and **d** $T = 8.23$. $T = 0$ correspond to the moment the slide box initiates movement. The origin shown is at the front gate of the retracted slide box along the landslide centerline

decayed towards gravity as the slide box travelled downslope given the limited airflow supplied to the large diameter and long stroke pistons. The average acceleration from launch until slide release ranged from 0.8 to 1.6g. Abrupt peak deceleration spikes of the empty slide box of up to $-12g$ allowed the landslide material to empty the box and continue sliding down the hill slope under the effect of gravity.

Table 1 Summary of absolute value of errors in the image measurements

Errors	Above water camera	PIV camera
Image rectification	1.5 pixel	2.2 pixel
ϵ_x, ϵ_y	1.35 mm	1.8 mm
ϵ_t	5 ms	–

Granular landslide instrumentation

Multiple camera setup

A total of 12 digital video cameras were placed in and around the wave basin to record the landslide motion from its inception

Table 2 Maximum uncertainty in the experimental measurements of the non-dimensional landslide impact parameters

Non-dimensional landslide parameter	Uncertainty (%)
$F_s = v_s / \sqrt{g s_0}$	5.3
$S = s/s_0$	3.0
$B = b/s_0$	6.2
$V = V_s / (s_0^3)$	–

Table 3 Repeatability of the experiments based on identical trial runs with maximum initial pneumatic launch pressure $P = 10$ bar

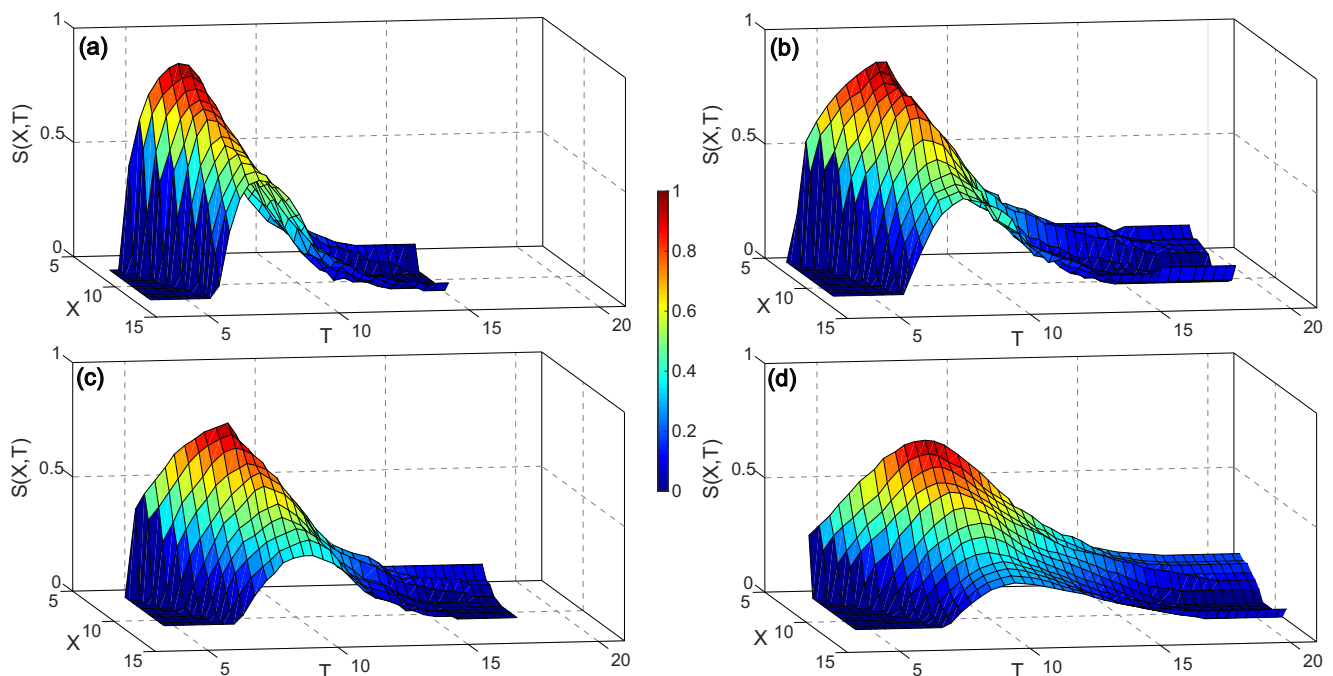
Parameter	Dimension	Run 1	Run 2	Planar hill slope			Δ	Conical hill slope		Δ
				Run 3	Run 4	Run 5		Run 1	Run 2	
h	[m]	0.60	0.58	0.60	0.60	0.59	0.02	0.302	0.303	0.001
v_s	[m/s]	5.33	5.33	5.29	5.32	5.28	0.05	6.60	6.63	0.03
s	[m]	–	–	0.215	0.217	0.224	0.009	0.139	0.144	0.005
b	[m]	1.886	1.91	1.914	1.961	1.892	0.075	3.02	2.98	0.04
V_s	[m ³]	0.756	0.756	0.756	0.756	0.756	0	0.378	0.378	0

to the final deposition at the bottom of the TWB. The cameras were calibrated by means of calibration boards with uniform dot matrix patterns. The calibration and rectification model follows a pin-hole mapping model (Hartley and Zissermann 2000), which is based on the theorem of intersecting lines. Significant calibration board coverage across the field of view allows extrapolation of the calibration over the entire field of view through the pin-hole model. The images are corrected for barrel distortions and the magnification factors relating the pixel scale to the slope coordinates are obtained. The slide front velocity v_s , thickness s , and width b are measured from the corrected video image sequences. The slide front velocity and width are measured by tracking the location of the slide front in the image sequence. Slide thickness is measured as a function of location and time during the entire duration of slide motion from the image sequence recorded by the above water side view cameras (Fig. 3). It is further corroborated with surface reconstruction using the stereo particle image velocimetry (PIV) camera system on the conical hill slope. The slide width is measured by tracking the

location of the lateral slide extent on the slope from the image sequences recorded by the PIV camera.

Particle image velocimetry

Two different PIV systems were used. A planar PIV system consisting of a single CCD camera was used for the planar hill slope to measure the landslide surface kinematics. The increased lateral spreading of the landslide on the conical hill slope required a stereo PIV system consisting of two CCD cameras to measure the landslide kinematics and perform surface reconstruction. The high resolution CCD cameras used were Pro Plus 2M CCD progressive-scan-camera with an image resolution of 1600×1200 pixel at up to 30 frames per second provides double shutter capabilities for back-to-back frame recordings suitable for cross-correlation analysis. The planar configuration mounted the single camera on a framework 6.9 m overhead perpendicular to the hill slope and above the water surface providing approximately a 15.4 m^2 ($4.53 \text{ m} \times 3.40 \text{ m}$) viewing area of the hill slope in the impact region. The stereo configuration mounted the two

**Fig. 4** Landslide shape evolution along the hill slope for $V = 28$ and slide box Froude number F_b of **a** 2.16, **b** 1.86, **c** 1.63, and **d** 1.34

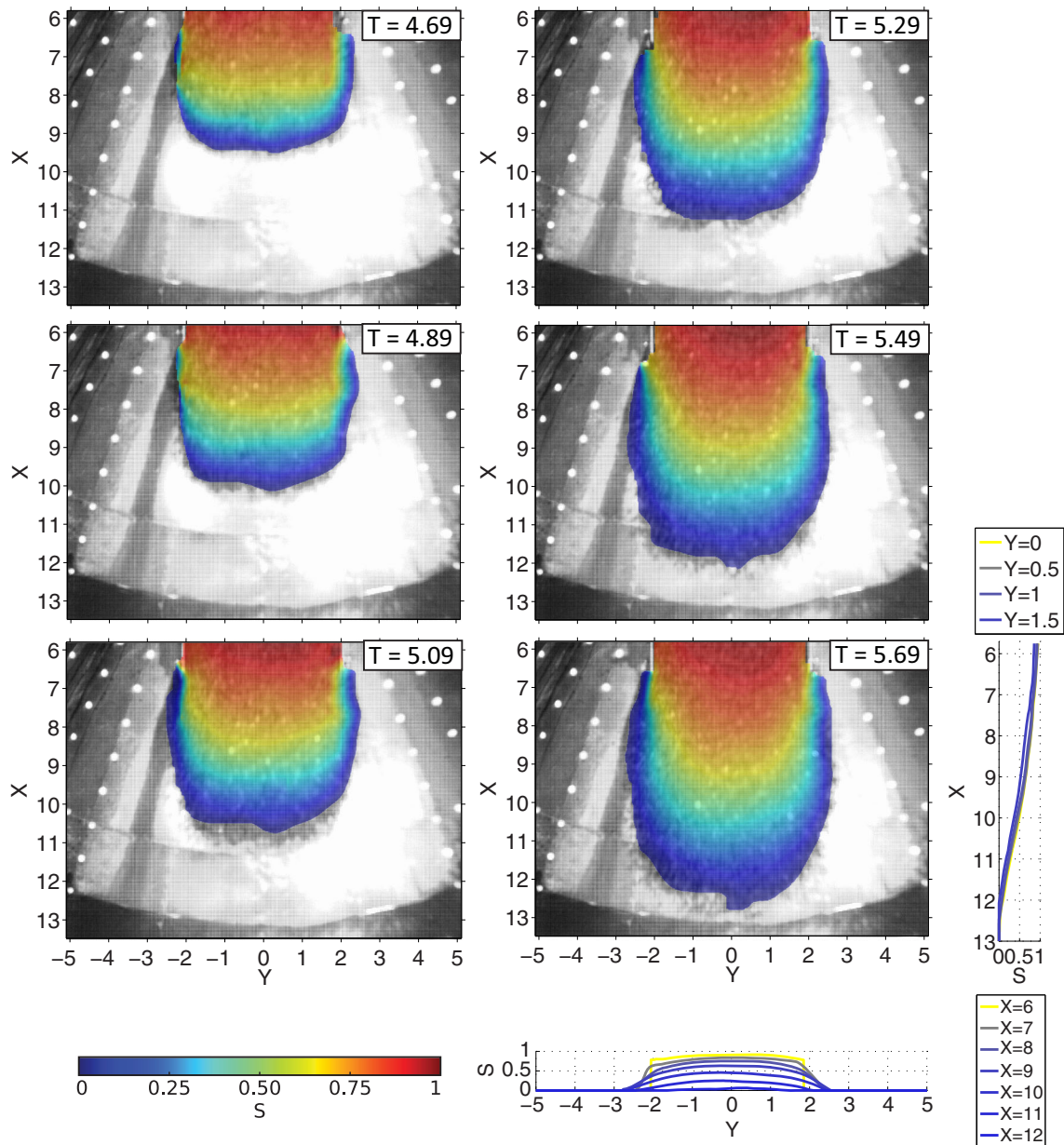


Fig. 5 Landslide thickness sequence reconstructed using the stereo PIV camera system for a gravel landslide volume $V = 28$ and slide box Froude number $F_b = 2.16$ on the conical hill slope

CCD cameras 3.30 m apart creating a 26° angle between the two cameras at the landslide center axis. The cameras were mounted 7.35 m normal to the conical hill slope with an approximate viewing area of 16.4 m^2 ($4.67 \text{ m} \times 3.50 \text{ m}$). The digital image acquisition, PIV analysis, and landslide surface reconstruction are performed with the FlowMaster PIV and StrainMaster DIC packages in the software DaVis (LaVision Inc., Göttingen, Germany). Single exposure images are acquired at frame rates of 15 and 30 fps in the experiments. The velocity distribution on the landslide surface is determined with an iterative multi-pass cross-correlation based particle image velocimetry (PIV) analysis applied to the speckle-like pattern produced by the granular slide surface (Fritz 2002b; Fritz et al. 2003a, b).

The PIV-processing and windowed Digital Image Correlation (DIC) are applied only to the subaerial stretch of the landslide motion prior to engulfment. The landslide flow fields are isolated from the hill slope background image and the water body during image preprocessing with digital masks (Roth et al. 1999; Lindken and Merzkirch 2000). The masking avoids biased or erroneous correlation signals caused by total reflections and light scattering on the hill slope, water surface, and splash during the impact. The cross-correlation based analysis is conducted on the planar and conical hill slopes by customizing a commercial PIV analysis software (LaVision Inc., DaVis FlowMaster PIV package). The advanced digital interrogation method successfully combines several techniques: cross-correlation analysis (Keane and Adrian 1992), discrete

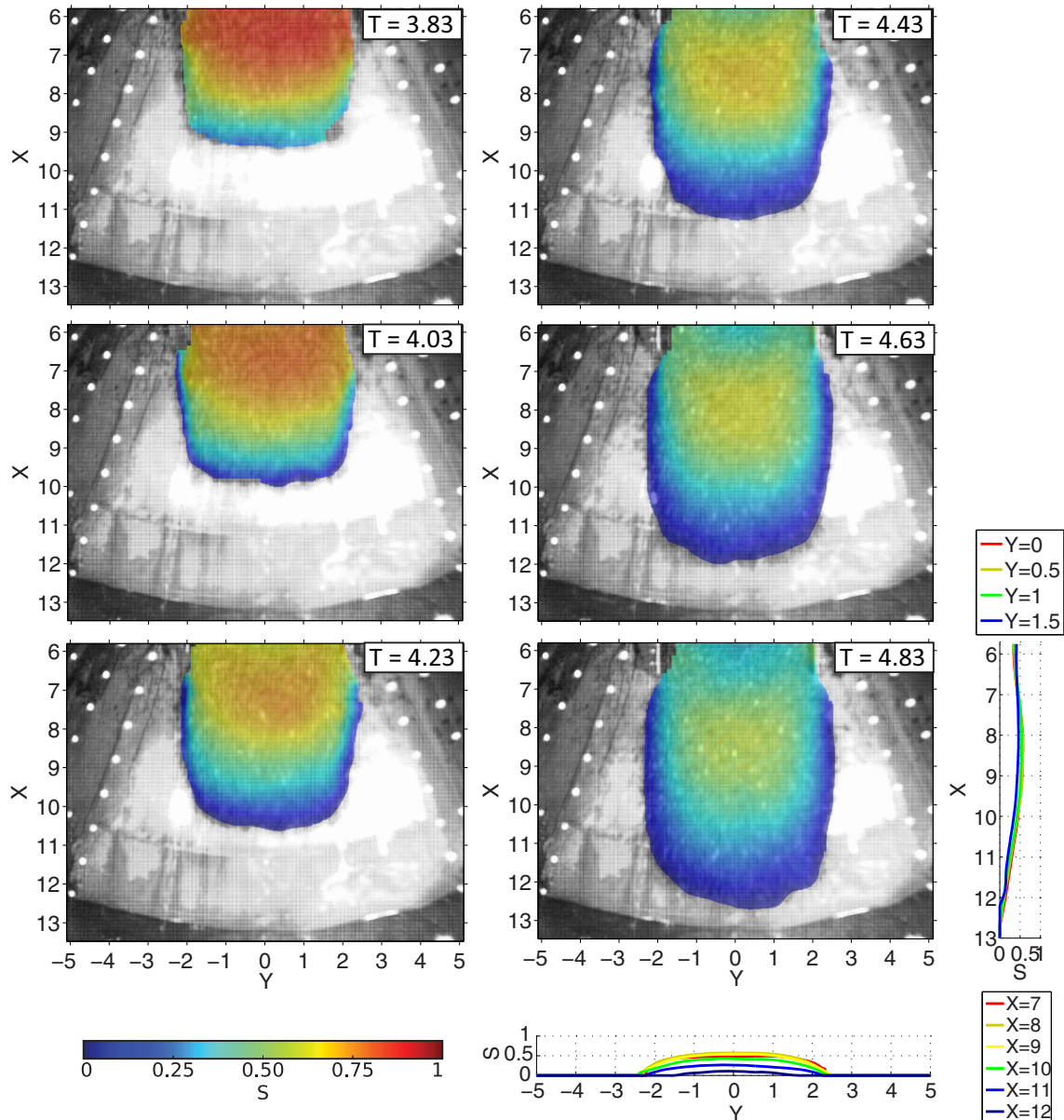


Fig. 6 Landslide thickness sequence reconstructed using stereo PIV system for a gravel landslide volume $V = 14$ and slide box Froude number $F_b = 2.33$ on the conical hill slope

window offset (Westerweel et al. 1997), fractional window offset (Scarano and Riethmuller 2000), iterative multi-grid processing with window refinement (Hart 1998; Scarano and Riethmuller 1999), and window distortion (Huang et al. 1993a, b; Fincham and Delerce 2000). The adaptive multi-pass algorithm initially calculates a reference vector field from the double image input. A standard cross-correlation interrogation is then performed with a relatively large interrogation window size (128×128 pixels) and a mean initial window shift. The calculated velocity field serves as initial displacement for the multi-pass cross-correlation algorithm to predict the velocity for the next iteration. This velocity prediction determines the window shift for the next higher resolution level with a refined interrogation window size. The iteration is repeated until the final window size (32×32 pixels) is reached. The PIV analysis is limited to image

sequences with adequate speckle-like patterns on the granular slide surface, which is required for an accurate identification of the peak shift in the correlation plane.

Imaging measurement accuracy

The uncertainty in experimental measurements arises due to systematic and random errors. Since most of the landslide measurements are based on the camera recordings, the uncertainty in the camera image measurements is estimated. The errors from the camera measurements may be summarized as $\epsilon_{tot} = \epsilon_{\nu} + \epsilon_{optics}$, where ϵ_{ν} is the random error and ϵ_{optics} is the optical imaging error. The random errors arise due to the interrogation technique, which can include an algorithm or manual collection of data points from the image sequences. The optical imaging error arises

due to the recording, image rectification, and calibration process. In PIV, additional errors are introduced ε_{bias} and a particle flow tracking error ε_{track} . Based on the image calibration, the errors in image rectification and spatial landslide measurements from imagery are summarized in Table 1. The maximum error for the PIV analysis has been estimated based on a combination of numerical simulations with synthetic images and benchmark cases (Huang et al. 1997; Raffel et al. 1998; Westerweel 2000). The absolute maximum error of the displacement vector in the experiment is found as $\varepsilon_{tot} < 0.02$ m/s. Since the PIV analysis involves an adaptive multi-pass algorithm with window deformation, the bias error in vector displacements can be neglected $\varepsilon_{bias} \approx 0$ (Scarano and Riethmuller 2000). The landslide granulate itself provides the particles for the landslide velocity flow estimation. Hence, the “flow fidelity” error in the particle tracking can be neglected, $\varepsilon_{track} \approx 0$. The random displacement error can be conservatively assumed as $\varepsilon_x = 0.1$ pixels, allowing the minimum resolvable displacement fluctuation (Raffel et al. 1998; Scarano and Riethmuller 2000). Then, the random error in velocity measurement can be estimated as $\varepsilon_v \leq 0.004$ m/s for the constant frame rate of the image recordings. The random error in velocity measurements changes with the temporal and spatial resolutions. Additional errors in the PIV analysis may arise due to the out-of-plane motion of the landslide mass. As the landslide spreads down the hill slope, the thickness of the landslide decreases. The motion of the granular particles is downward and outward with reference to the plane of the hill slope. On the planar hill slope, the maximum change in the landslide thickness over the measured range is approximately 0.15 m. This corresponds to an estimated 2% change in the observation distance between the measured landslide surface and the camera position. Thus, errors due to out-of-plane motion of the granular landslide on the planar hill slope are marginal and the granular landslide surface is considered as a planar surface for the PIV analysis. The uncertainty in the surface reconstruction has been estimated based on several benchmark cases of DIC algorithm by Orteu et al. (1997), Garcia et al. (2002), and Chen et al. (2013). The correlation algorithm was accurate to 1/100 pixels, and the ideal grid intersection extraction accuracy was 1/30 pixels. Considering the relatively large scale of the application and absolute error according to camera resolution, the accuracy in landslide thickness and width in this technique is estimated as 5%. On the conical hill slope, the change in landslide thickness in the slide centerline is comparable to the planar scenario, but the increased lateral spreading on the convex conical slope requires the use of a stereo PIV system to include the out-of-plane motion of the landslide. Based on the absolute errors, the maximum uncertainty in the experimental measurements of non-dimensional landslide parameters that govern wave generation is summarized in Table 2. By conducting multiple experimental trials with the same parameters, the repeatability of the landslide motion is estimated. The repeatability is summarized in Table 3.

Granular landslide motion

Landslide shape

The landslide shape is characterized by measurements of slide thickness $S(X, T)$ at the centerline and width $B(X, T)$ during the subaerial landslide motion as shown in Fig. 4. The shape functions for the landslide volume $V=28$, corresponding to a mass $m_s =$

1350 kg, and the landslide release Froude numbers $F_b = 2.16, 1.86, 1.63,$ and 1.34 are obtained by combining the measured data from different experimental trials with the same pneumatic settings. $X=0$ corresponds to the initial static position of the landslide front and $T=0$ corresponds to the initiation of box motion. The landslide shape is characterized by a peak thickness exiting the slide box and a gradual decay in the thickness with propagation down the hill slope and with time. As the granular landslide propagates down the hill slope, it experiences unconfined spreading in both longitudinal and transverse directions. The reconstructed landslide surface on the conical hill slope shows the landslide shape can be characterized by a gradual decrease from the peak thickness exiting the slide box to the leading front. The thickness distribution in the lateral direction is measured in the stereo PIV analysis. The lateral thickness distribution transits from trapezoidal near the slide box exit to parabolic at downstream locations as seen in Figs. 5 and 6. The curvature of parabolic shape becomes larger as well as flatter with position downhill.

The maximum thickness $S_m(X)$ evolution along the planar and conical hill slopes is shown in Fig. 7 for $V=28$. After the landslide collapse from the box, the rate of decay of the landslide profile depends on the extent of the landslide spreading, which is mainly controlled by the rates of mass and momentum flux of the granular material in the direction of the slide motion. The evolution of the maximum landslide width $B_m(X)$ is shown in Fig. 7. On the planar hill slope, the granular material exits the landslide box and it spreads rapidly until the maximum lateral extent is approached asymptotically. Compared with planar slope, the landslides on the conical hill slope have larger lateral spreading width. On the conical hill slope, the landslide width continues to increase linearly with propagation down the hill slope. Fitting the experimental measurements, the linear maximum landslide width on the conical hill slope follows the form

$$B_m = (4 + m_b X + c_b) \quad (5)$$

where m_b is the lateral spreading function and c_b is a non-linear function of the landslide discharge from the slide box. The lateral spreading and discharge functions for the gravel landslide on the conical hill slope is given as

$$m_b = 0.4 F_s^{-0.08} S_m^{-0.05} V^{0.2} \quad (6)$$

and

$$c_b = -0.2 F_s^{0.7} S_m^{0.1} V^{0.6} \quad (7)$$

Likewise, the lateral spreading and discharge functions for the cobble landslide on the conical hill slope is given as

$$m_b = 0.8 F_s^{-0.7} S_m^{-0.2} V^{0.1} \quad (8)$$

and

$$c_b = -0.8 F_s^{-0.7} S_m^{-0.2} V^{0.5} \quad (9)$$

The predictive equations for the maximum landslide width result in an r^2 correlation coefficient of 0.99 for both landslide

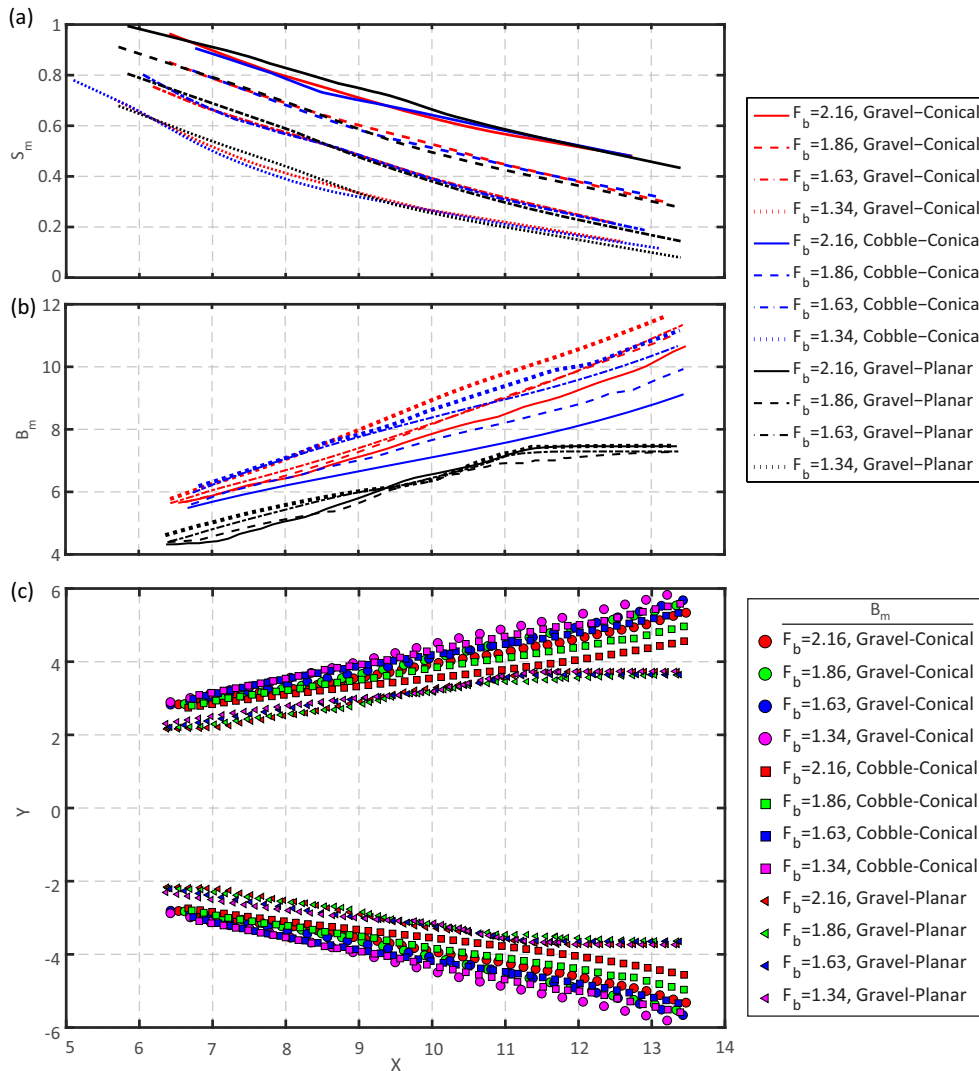


Fig. 7 Maximum landslide a thickness S_m and b width B_m , on the planar and conical hill slopes for $V = 28$ and slide box Froude number $F_b = 2.16, 1.86, 1.63,$ and 1.34 . c Maximum lateral spread of the landslide material down the hill slope

materials. The lateral spreading function is inversely proportional to the slide velocity and thickness, meaning rapid, thick landslides tend to have reduced maximum landslide width. For application to the field, the thickness and volume of potential landslide hazards on steep slopes are often estimated and the landslide velocity can be predicted by estimating the equivalent friction coefficient (Heim 1932; Scheidegger 1973; Hampton et al. 1996; Fritz 2002a) and applying it to the Newtonian laws of motion. As with all empirical equations, the applicability of these equations are limited to the range of conditions tested.

Landslide velocity

The landslide front velocity is measured from videos of the PIV and above water side cameras. The landslide front velocity coincides approximately with the measured slide box velocity up to the release point. The landslide exits at the peak slide box velocity as the box deceleration is initiated. The slide release corresponds to the transformation of a confined block-like slide to a

granular avalanche. The landslide release velocity is approximated by the maximum slide box velocity. All the measured slide front velocities are shown with the slide box velocity in Fig. 2. The front velocity measured from the PIV analysis has an average 3% deviation from the manual tracking based front velocity. The measured front velocity depends on the release velocity, landslide mass, and landslide release location. The slide release Froude number for the landslide volumes $V = 28$ and 14 ($m_s = 1350$ and 675 kg) was in the range $1.3 \leq F_b \leq 2.2$ and $1.2 \leq F_b \leq 2.4$, respectively, corresponding to slide box release velocity ranges of $2.3 \text{ m/s} \leq v_b \leq 3.7 \text{ m/s}$ and $2.2 \text{ m/s} \leq v_b \leq 4.0 \text{ m/s}$, respectively. The slide front Froude number at impact is in the range $2.2 \leq F_s \leq 3.8$ corresponding to a slide impact velocity of $3.7 \text{ m/s} \leq v_s \leq 6.6 \text{ m/s}$. Along with the landslide shape, the front velocity is critical for tsunami wave generation and predicting the tsunami wave characteristics in terms of the landslide parameters (Fritz 2002a; Walder et al. 2003; Panizzo et al. 2005; Zweifel et al. 2006; Di Risio et al. 2009; Heller and Hagar 2010; Mohammed 2010;

Mohammed and Fritz 2012, 2013; McFall 2014; McFall and Fritz 2016, 2017; Romano et al. 2016; Bregoli et al. 2017).

The surface velocity distribution U_s for a run with landslide volume $V=28$ and slide box Froude number or $F_b=2.16$ on the planar hill slope are shown in Fig. 8. The surface velocity maximum is at the centerline with corresponding peak landslide thickness. The velocity decreases towards the lateral edge of the landslide on the hill slope. After the landslide release from the box, the peak surface velocity magnitude increases as the gravity driven landslide plunges downhill.

The initial acceleration of the confined landslide, location of the landslide release, and transformation into a granular avalanche affect the landslide shape distribution, mass, momentum, and energy flux rates as the slide plunges downhill. The surface velocity

distribution at impact of the landslide with the water surface is shown in Fig. 8. The longitudinal and lateral deformations of the granular slides vary with the launch velocity of the slide volume. Landslides with higher launch velocity tend to maintain their shape for a longer duration of the motion and thus display less deformation along the hill slope, when compared with the same landslide with lower release velocities. The large spread and low velocity of the landslide front for the low initial acceleration cases result in lower landslide thickness at impact from conservation principles.

Figure 9 shows the stereo PIV measurement of the slide released on the conical hill slope. The panels have a constant time step, and the last frame shows the moment before impact of the landslide with the water surface. The color map of the vector fields

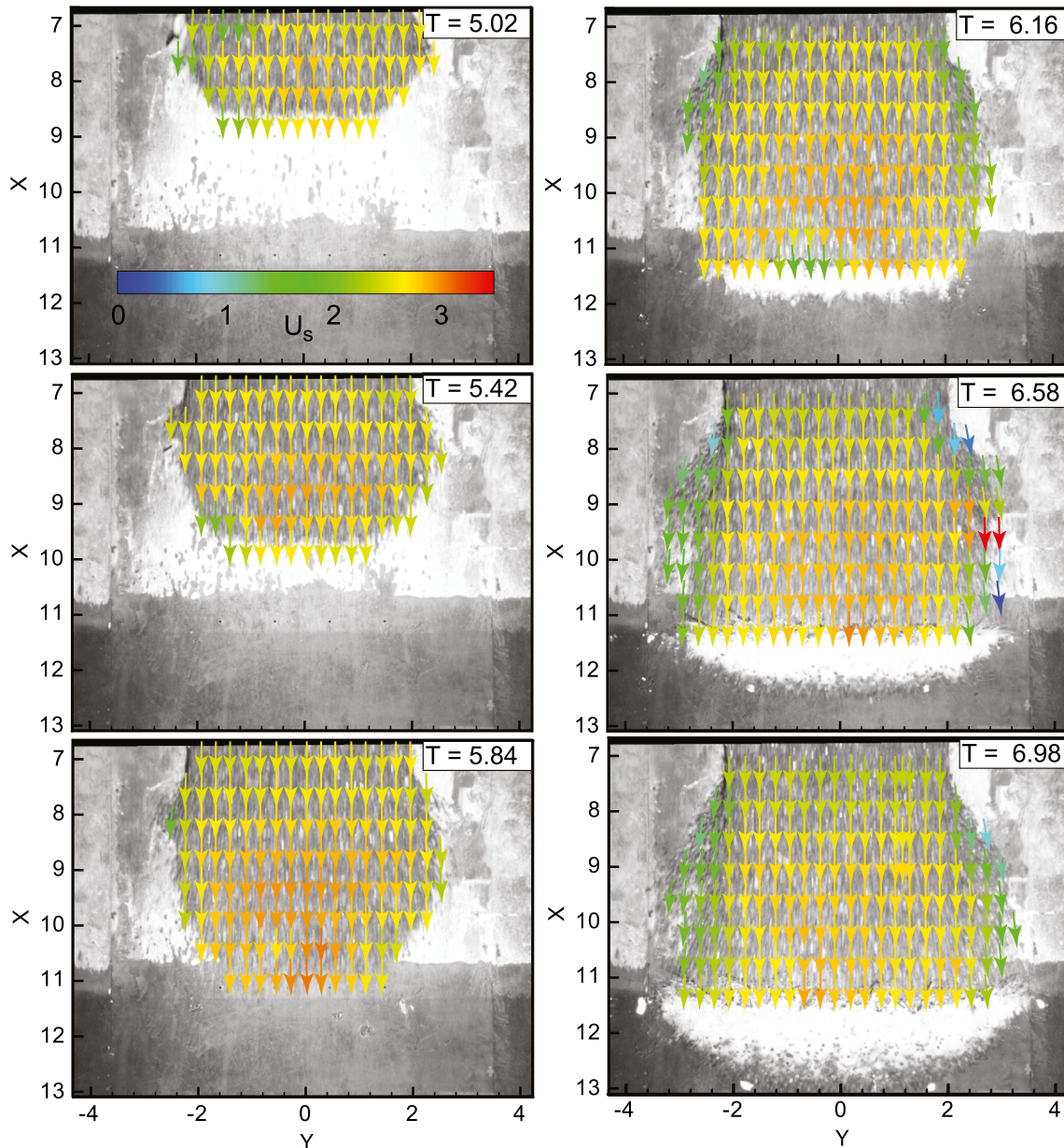


Fig. 8 PIV surface velocity vector map sequence for a gravel landslide with $V=28$ and slide box Froude number $F_b=2.16$ on the planar hill slope

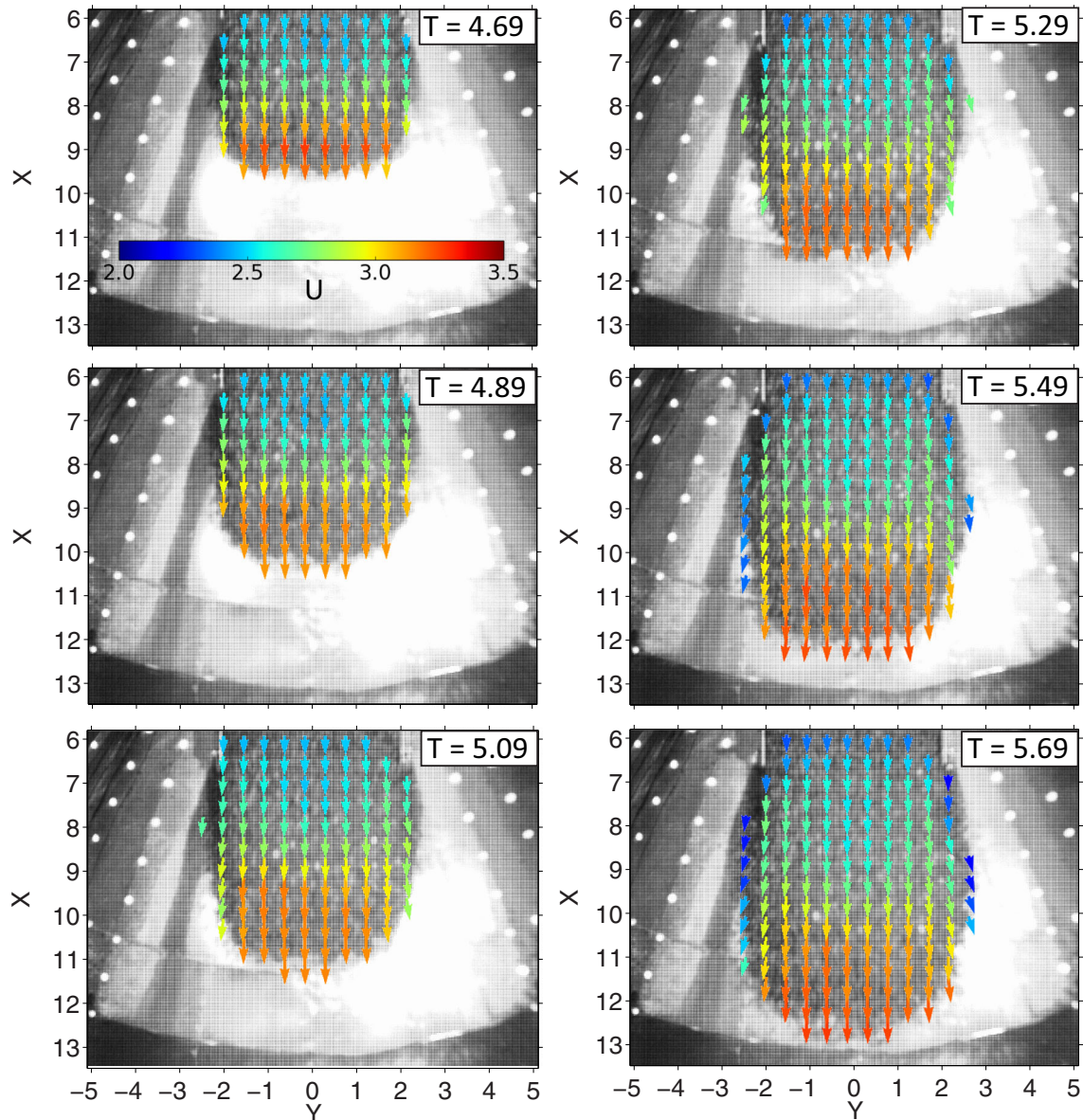


Fig. 9 Stereo PIV velocity vector map sequence for a gravel landslide with $V = 28$ and slide box Froude number $F_b = 2.16$ on the conical hill slope

is the normalized magnitude of the velocity components in three directions. The spatial distribution of the velocity magnitude at impact with the water surface is in the range of $2.3 \leq U \leq 3.3$. The dominant velocity component is in downhill direction with the maximum velocity at the landslide front.

Velocity components in all three directions follow a symmetric distribution about the centerline. The lateral (y) and vertical (z) velocity components are almost one order smaller than the longitudinal (x) one. The relation between the velocity components in the calculated time period is given as

$$\begin{aligned} 0 \leq U_y/U_x &\leq 0.2 \\ 0 \leq U_z/U_x &\leq 0.32 \end{aligned}$$

The lateral component shows the width spreading of landslide material and monotonous increase with distance from the

centerline until reaching the lateral slide envelope. Once the landslide shape is fully developed, the median value of the lateral velocity component approaches an asymptotic relation with the longitudinal component, $M(U_y/U_x) \approx 0.04$. The vertical component decreases over time with a maximum magnitude at the initiation of spreading. Prior to engulfment, the vertical velocity reaches an asymptotic relation, $M(U_z/U_x) \approx 0.11$. These relations between the velocity components highlight the dominance of the downhill component in the main body of the landslide.

The longitudinal and lateral components in stereo PIV results can be directly compared to 2D PIV results by analyzing the images from an individual camera. Only 10% of longitudinal velocity vectors exceed 5% relative difference between the stereo and 2D PIV measurements, which are located near the peak thickness and the leading boundary. Similarly, 15% of the lateral

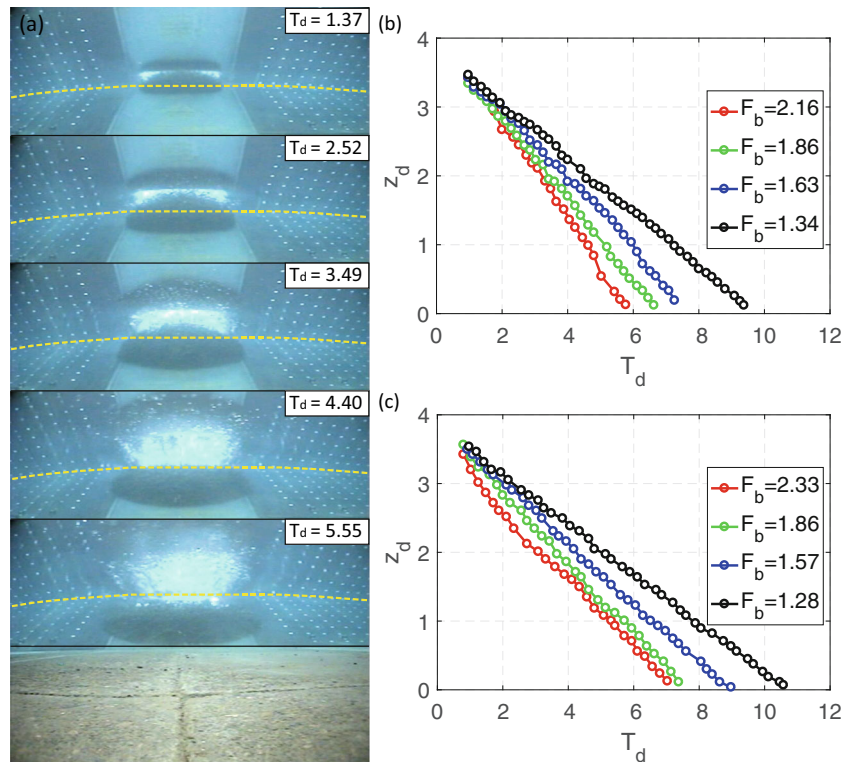


Fig. 10 Underwater landslide motion shown as **a** an underwater image sequence and vertical position of the subaqueous landslide front on the planar hill slope as a function of time for **b** $V=28$ and **c** $V=14$

velocity vectors exceed 5% relative difference, especially near the slide boundaries.

The stereo PIV analysis with the current camera setup has a good accuracy in longitudinal and lateral directions, but relatively poor accuracy in vertical direction. The anisotropic accuracy

characteristic is discussed in Brücker et al. (2012) and Kähler et al. (2016). Improved vertical accuracy could be attained with an increased number of cameras and multi-level calibration. The LSM algorithm used for measuring the 3D velocity field requires a high sampling frequency. With the current sampling rate, some

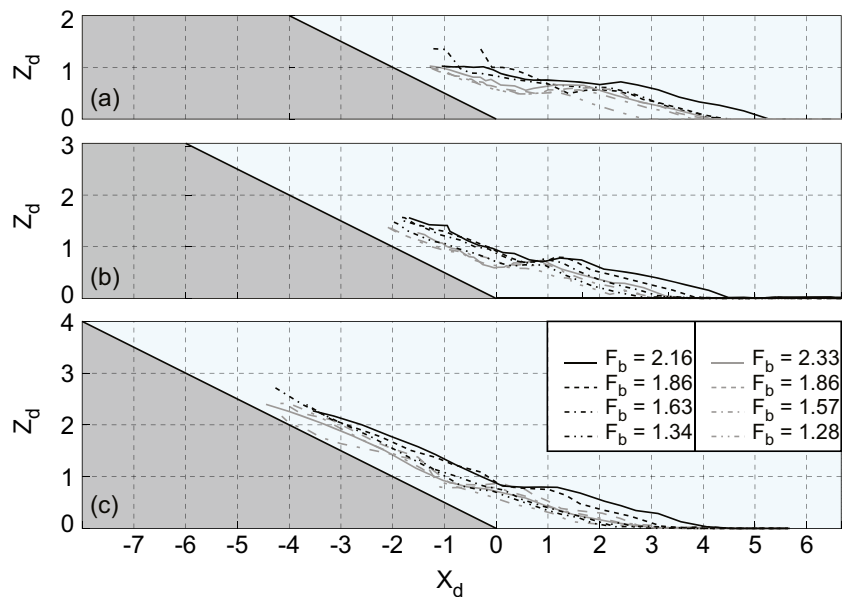


Fig. 11 Underwater granular landslide deposit profiles along the centerline of the planar hill slope at water depths, $H=$ **a** 2, **b** 3, and **c** 4 times the initial slide thickness s_0

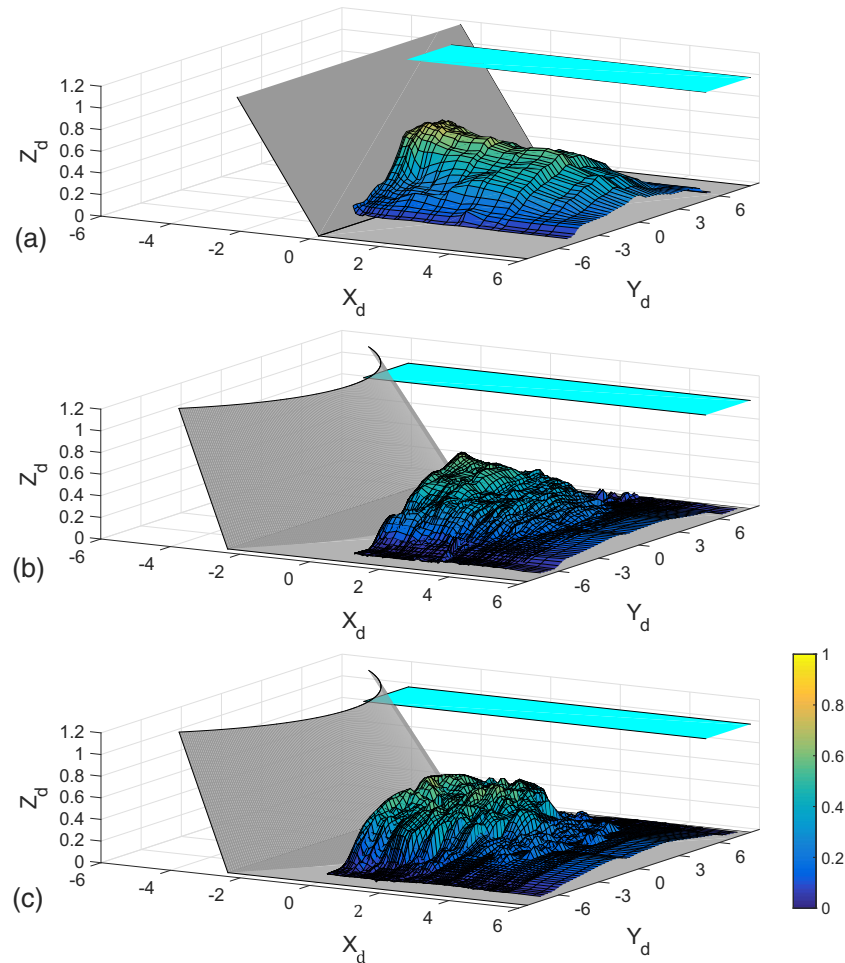


Fig. 12 Measured landslide deposit from landslide volume $V = 14$ and slide box velocity $F_b = 2.33$ for **a** gravel on a planar hill slope, **b** gravel on a conical hill slope, and **c** cobble on a conical hill slope

areas in the high gradients near the boundary of the landslide dropped out, which resulted in approximately 85% coverage of on the landslide surface. The validation of boundary velocity components has been corroborated with the measured velocity data from the side cameras (Fig. 3).

Submarine motion and landslide deposits

The submarine landslide front velocity is measured with underwater cameras and the landslide deposits are recorded with a multi-transducer acoustic array (MTA) after each experimental run. The submarine measurements are described with reference to a coordinate system following the wave basin coordinate system with origin at the toe of the hill slope (normalized by the initial slide thickness s_0) denoted by a subscript d (x_d, y_d, z_d), and $T_d = 0$ when the landslide impacts the water surface. The submarine landslide motion and measured front position are shown in Fig. 10. The linear trend of the measured submarine landslide front indicates a nearly constant front velocity along the submarine planar hill slope. The measured submarine velocity is approximately 50% of the corresponding subaerial landslide front velocity before impact. Upon impact with the water surface, the landslide decelerates rapidly due to water body energy transfer and wave

generation, energy losses due to surface skin friction and form drag, multi-phase mixing in the impact region, basal friction, internal losses due to deformation, buoyancy force, and saturation of the granular medium.

Once the landslide reaches the basin floor, the landslide spreads laterally in the runout zone into a scree fan shaped deposit characterized by a raindrop shaped outline with a wide front and reducing tail width towards the rear. The deposit profiles measured along the landslide centerline are shown in Fig. 11. The profiles are truncated at the tail end of the slide shape due to the requirement of sufficient submergence and standoff distance for the MTA. The runout distances from the toe of the planar slope is inversely related to the water depth with the largest runout occurring at the shallowest water depth. The thickness gradually increases from the tail until it reaches the flat bottom of the basin. The sharp transition between the hill slope and the flat bottom deflects and decelerates the landslide resulting in a bulging of the granular material. Beyond this point, the thickness decreases towards the front of the deposit. The impact velocity, slide volume, and water depth influence the location of the granular mass pileup and landslide runout distance on the basin floor.

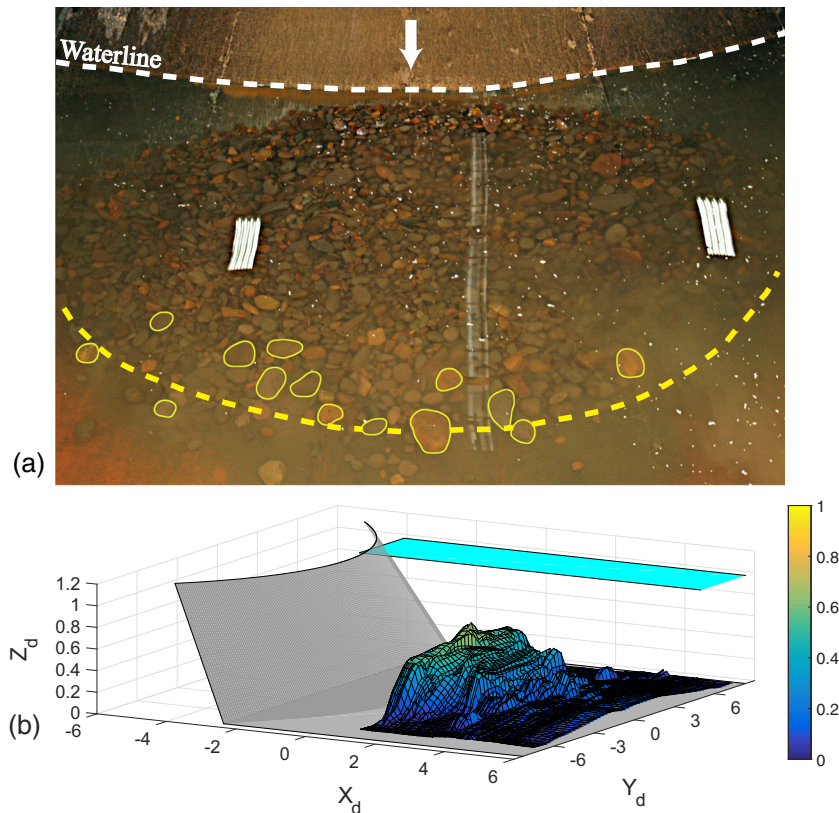


Fig. 13 Cobble landslide deposit on a convex conical hill slope with volume $V = 14$ and slide box velocity $F_b = 2.33$. **a** Overhead view of the landslide deposit with highlighted large cobbles near the maximum slide runout (Note the increased grain diameter with increased runout distance). **b** Measured landslide deposit

Measured underwater deposits for a gravel landslide on planar and conical hill slopes and cobble landslide on a conical hill slope are shown in Fig. 12 for $V = 14$ at water depth of $H = 1$ (0.3 m). Similar runout distance was observed with gravel landslides on planar and conical hill slope. The gravel landslide produces a much smoother deposit compared to the cobble landslide. The cobble landslide deposit becomes less smooth with increased distance from the hill slope, producing hummock type features near the maximum runout length. Hummocks and rigid “Toreva Blocks” are characteristically transported by volcanic debris avalanches and other large landslides and typically create a blocky surface on the landslide deposit (Voight et al. 1981, 1983; Moore et al. 1989; Glicken 1996). The decreased deposit smoothness with increased runout distance appears to qualitatively correlate to an increased grain diameter with runout distance as observed in Fig. 13. This may be caused by differential acceleration of granulates within the landslide material due to the irregular granulometry of the cobble landslides, and the larger cobbles are less susceptible to frictional forces.

Tsunami wave generation

Tsunami waves are generated by landslides through a rapid transfer of momentum from the landslide mass to the water body during the impact, penetration, and subaqueous runout. The displaced water, which moves primarily in the direction of the landslide and laterally around the landslide front, develops

into the leading radial wave front. When the drawdown of the water surface reaches the maximum, the restoring gravitational forces drive the water surface rebound. The subsequent runup and rundown on the hillslope form the second wave of the radial wave fronts. Subsequent oscillations of the shoreline form the trailing wave train. Lateral edge waves on the hill slope result from transverse displacement of water. The leading wave is generated by the initial slide impact and is strongly dependent on the slide front velocity and thickness at impact. The slide width and length affect the generation of the trailing waves. The measured landslide shape and kinematics provide source data characterize the resulting tsunami waves with developed empirical predictive equations (Mohammed and Fritz 2012, 2013; McFall and Fritz 2016, 2017).

Discussion and summary

A novel pneumatic landslide tsunami generator is deployed to launch unconfined granular landslides on planar and conical hill slopes. The experiments mimic natural landslides with an initial solid block motion, followed by disintegration of a landslide to collapse into a debris avalanche on a hill slope. Landslides consisting of naturally rounded river gravel with different volumes are launched at varying initial speeds on planar and conical hill slopes, and cobble landslides are launched on the conical hill slope. During the slide motion, measurements are made relating to slide shape, kinematics, and deposits to quantify the slide motion on the hill slope. Landslide observations

focus on source characterization for tsunami wave generation and propagation. The key parameters are the landslide thickness, width, front velocity, and landslide surface velocity. The varying launch pressures lead to varying slide box velocities at the release of the landslide. The different launch velocities result in different slide release locations, which cause variations in decay of maximum slide thickness along the hill slope. On the planar hill slope, the maximum landslide width downhill is approached asymptotically. The maximum width is larger on the conical hill slope compared to the planar hill slope. On the conical hill slope, the maximum width increases linearly with propagation down the hill slope, and empirical equations have been derived for the maximum width on the conical hill slope. The slide thickness has been measured using image processing from side cameras and using landslide surface reconstruction using the stereo PIV system on the conical hill slope. The PIV velocity measurements provide a valuable data source for describing the slide kinematics on the planar and conical hill slopes. The surface slide velocity reaches a maximum at the slide front. Across the slide width, the maximum surface velocity occurs at the midsection of the landslide where the thickness is the maximum. The slide front velocity increases with increasing slide launch velocity and increases along the hill slope as the slide disintegrates and travels downhill under the influence of gravity. The slide deposits are affected by the water depth in the wave basin and the impact characteristics of the slide with the water surface. The cobble landslide deposit is less smooth with increased distance from the hill slope, producing hummock type features near the maximum runout length. These measurements overall provide a valuable source for understanding landslide dynamics on planar and conical hill slopes. Additionally, they can be used for benchmarking advanced numerical simulations of granular landslides as well as input for empirical predictions of landslide generated tsunami wave characteristics.

Acknowledgements

The data from this study may be obtained at data depot of the DesignSafe-CI website at www.designsafe-ci.org.

Funding information This work was supported by the National Science Foundation (NSF), Division of Civil, Mechanical and Manufacturing Innovation awards: CMMI-0421090, CMMI-0936603, CMMI-0402490, CMMI-0927178, and CMMI-1563217; the U.S. Department of Defense (DoD) through the Science, Mathematics and Research for Transformation (SMART) fellowship; and the U.S. Army Corps of Engineers through the Coastal Inlet Research Program (CIRP).

References

- Ataie-Ashtiani B, Najafi-Jilani A (2008) Laboratory investigations on impulsive waves caused by underwater landslide. *Coast Eng* 55(12):989–1004. <https://doi.org/10.1016/j.coastaleng.2008.03.003>
- Bardet J-P, Synolakis C, Davis H, Imamura F, Okal E (2003) Landslide tsunamis: recent findings and research directions. *Pure Appl Geophys* 160:1793–1809
- Bondevik S, Løvholt F, Harbitz C, Mangerud J, Dawson A, Svendsen J (2005) The Storegga slide tsunamis comparing field observations with numerical solutions. *Mar Pet Geol* 22:195–208
- Bregoli F, Bateman A, Medina V (2017) Tsunamis generated by fast granular landslides: 3D experiments and empirical predictors. *J Hydraul Res* 55:743–758. <https://doi.org/10.1080/00221686.2017.1289259>
- Brücker C, Hess D, Kitzhofer J (2012) Single-view volumetric PIV via high-resolution scanning, isotropic voxel restructuring and 3D least-squares matching (3D-LSM). *Meas Sci Technol* 24(2):024001
- Buffington JM, Dietrich WE, Kirchner JW (1992) Friction angle measurements on a naturally formed gravel streambed: implications for critical boundary shear stress. *Water Resour Res* 28:411–425. <https://doi.org/10.1029/91WR02529>
- Chen F, Chen X, Xie X, Feng X, Yang L (2013) Full-field 3D measurement using multi-camera digital image correlation system. *Opt Lasers Eng* 51(9):1044–1052
- Crosta GB, Imposimato S, Roddeman D (2016) Landslide spreading, impulse water waves and modelling of the Vajont rockslide. *Rock Mech Rock Eng* 49(6):2413–2436. <https://doi.org/10.1007/s00603-015-0769-z>
- Di Risio M, DeGirolamo P, Bellotti G, Panizzo A, Aristodemo F, Molfetta MG, Petrillo AF (2009) Landslide-generated tsunamis runup at the coast of a conical island: new physical model experiments. *J Geophys Res* 114:C01009. <https://doi.org/10.1029/2008JC004858>
- Enet F and Grilli ST (2005) Tsunami landslide generation: modeling and experiments. In *Proc 5th Int Conf on Ocean Wave Measurement*. Madrid, Spain: WAVES 2005
- Enet F, Grilli ST (2007) Experimental study of tsunami generation by three-dimensional rigid underwater landslides. *J Waterw Port Coast Ocean Eng* 133(6):442–454
- Fincham AM, Delerce G (2000) Advanced optimization of correlation imaging velocimetry algorithms. *Exp Fluids* 29:513–522
- Fine I, Rabinovich A, Bornhold B, Thomson R, Kulikov E (2005) The grand banks landslide-generated tsunami of November 18, 1929: preliminary analysis and numerical modeling. *Mar Geol* 215:45–47
- Fritz HM (2002a) Initial phase of landslide-generated impulse waves. PhD thesis. Eidg. Tech. Hochsch, Zürich, Switzerland
- Fritz HM (2002b) PIV applied to landslide generated impulse waves. In: Adrian RJ et al (eds) *Laser techniques for fluid mechanics*. Springer, Berlin, pp 305–320
- Fritz HM, Moser P (2003) Pneumatic landslide generator. *Int J Fluid Power* 4(1):49–57
- Fritz HM, Hager WH, Minor H-E (2001) Lituya bay case: rockslide impact and wave runup. *Sci Tsunami Haz* 19(1):3–22
- Fritz HM, Hager WH, Minor H-E (2003a) Landslide generated impulse waves. 1. Instantaneous flow fields. *Exp Fluids* 35:505–519
- Fritz HM, Hager WH, Minor H-E (2003b) Landslide generated impulse waves. 2. Hydrodynamic impact craters. *Exp Fluids* 35:520–532
- Fritz HM, Hager WH, Minor H-E (2004) Near field characteristics of landslide generated impulse waves. *J Waterw Port Coast Ocean Eng* 130(6):287–302
- Fritz HM, Kongko W, Moore A, McAdoo B, Goff J, Harbitz C, Uslu B, Kalligeris N, Suteja D, Kalsum K, Titov V, Gusman A, Latief H, Santoso E, Sujoko S, Djulkarnaen D, Sunendar H, Synolakis C (2007) Extreme runup from the 17 July 2006 Java tsunami. *Geophys Res Lett* 34:L12602
- Fritz HM, Mohammed F, Yoo J (2009) Lituya Bay landslide impact generated megatsunami 50th anniversary. *Pure Appl Geophys* 166(1–2):153–175
- Fritz HM, Hillaire JV, Molière E, Wei Y, Mohammed F (2013) Twin tsunamis triggered by the 12 January 2010 Haiti earthquake. *Pure Appl Geophys* 170(9–10):1463–1474. <https://doi.org/10.1007/s00024-012-0479-3>
- Garcia D, Orteu JJ, Penazzi L (2002) A combined temporal tracking and stereo-correlation technique for accurate measurement of 3D displacements: application to sheet metal forming. *J Mater Process Technol* 125:736–742
- Genevois R, Ghirotti M (2005) The 1963 Vajont landslide. *Giorn Geol Appl* 1:41–52
- Glicken H (1996) Rockslide-debris avalanche of May, 18, 1980, Mount St. Helens volcano, Washington. U.S. Geological Survey. Open-File Report 96–677
- Gray JMNT, Wieland M, Hutter K (1999) Gravity-driven free surface flow of granular avalanches over complex basal topography. *Proc R Soc A* 455:1841–1874
- Greve R, Hutter K (1993) Motion of a granular avalanche in a convex and concave curved chute: experiments and theoretical predictions. *Phil Trans R Soc A* 342:573–600. <https://doi.org/10.1098/rsta.1993.0033>
- Grilli ST, Watts P (2005) Tsunami generation by submarine mass failure. I: modeling, experimental validation, and sensitivity analysis. *J Waterw Port Coast Ocean Eng* 131(6):283–297
- Hampton MA, Lee HJ, Locat J (1996) Submarine landslides. *Rev Geophys* 34(1):33–59. <https://doi.org/10.1029/95RG03287>
- Hart DP (1998) Super-resolution PIV by recursive local correlation. In *Proc Intl Conf Optical Tech and Image Processing in Fluid, Thermal and Combustion Flow*. Yokohama, Japan. VSJ-SPIE98, AB149: 167–180
- Hartley R, Zissermann A (2000) Multiple view geometry in computer vision. Cambridge University Press, Cambridge

- Heim A (1882) Der Bergsturz von Elm. *Z Dtsch Geol Ges* 34:74–115 (in German)
- Heim A (1932) Bergsturz und Menschenleben. Fretz und Wasmuth, Zürich (in German)
- Heller V, Hager WH (2010) Impulse product parameter in landslide generated impulse waves. *J Waterw Port Coast Ocean Eng* 136:145–155. [https://doi.org/10.1061/\(ASCE\)WW.1943-5460.0000037](https://doi.org/10.1061/(ASCE)WW.1943-5460.0000037)
- Hendron AJ, Patton FD (1985) The Vaiont slide, a geotechnical analysis based on new geologic observations of the failure surface. US Army Corps of Engineers Technical Report GL-85-5 (2 volumes)
- Hsü KR (1975) Catastrophic debris streams (sturzstroms) generated by rockfalls. *Geol Soc Am Bull* 86(1):128–140
- Huang HT, Fielder HF, Wang JJ (1993a) Limitations and improvements of PIV. Part I: limitation of conventional techniques due to deformation of particle image patterns. *Exp Fluids* 15:168–174
- Huang HT, Fielder HF, Wang JJ (1993b) Limitations and improvements of PIV. Part II: particle image distortion, a novel technique. *Exp Fluids* 15:263–273
- Huang HT, Dabiri D, Gharib M (1997) On errors of digital particle image velocimetry. *Meas Sci Technol* 8:1427–1440
- Huber A (1980) Schwallwellen in Seen als Folge von Bergstürzen, VAW Mitteilung 47, Versuchsanstalt für Wasserbau, Hydrologie und Glaziologie, ETH Zürich
- Hutter K, Koch T (1991) Motion of a granular avalanche in an exponentially curved chute: experiments and theoretical predictions. *Phil Trans R Soc A* 334:93–138
- Hutter K, Koch T, Plüss C, Savage SB (1995) Dynamics of avalanches of granular materials from initiation to runout, part II: laboratory experiments. *Acta Mech* 109:127–165
- Iverson RM, Logan M, Denlinger RP (2004) Granular avalanches across irregular three-dimensional terrain. 2. Experimental tests. *J Geophys Res* 109:F01015
- Kähler CJ, Astarita T, Vlachos PP, Sakakibara J, Hain R, Discetti S, La Foy R, Cierpka C (2016) Main results of the 4th international piv challenge. *Exp Fluids* 57:97. <https://doi.org/10.1007/s00348-016-2173-1>
- Keane RR, Adrian RJ (1992) Theory of cross-correlation analysis of PIV images. *Appl Sci Res* 49:191–215
- Koch T (1989) Bewegung einer Granulatlawine entlang einer gekrümmten Bahn. Diplomarbeit. Technische Hochschule Darmstadt. 122 pp
- Koch T, Greve R, Hutter K (1994) Unconfined flow of granular avalanches along a partly curved surface. Part II. Experiments and numerical computations. *Proc R Soc A* 445:415–435
- Körner HJ (1983) Zur Mechanik der Bergsturzströme von Huascarán, Peru. *Hochgebirgsforschung* 6:71–110 (in German)
- Li Z, Komar PD (1986) Laboratory measurements of pivoting angles for applications to selective entrainment of gravel in a current. *Sedimentology* 33:413–423. <https://doi.org/10.1111/j.1365-3091.tb00545.x>
- Lindken R, Merzkirch W (2000) Velocity measurements of liquid and gaseous phase for a system of bubbles rising in water. *Exp Fluids* 29:S194–S201
- Locat J (2001) Instabilities along ocean margins: a geomorphological and geotechnical perspective. *Mar Pet Geol* 18:503–512
- Locat J, Lee HJ (2002) Submarine landslides: advances and challenges. *Can Geotech J* 39:193–212
- McFall BC (2014) Physical modeling landslide generated tsunamis in various scenarios from fjords to conical islands, PhD thesis, Ga. Inst of Tech, Atlanta
- McFall BC, Fritz HM (2016) Physical modelling of tsunamis generated by three-dimensional deformable granular landslides on planar and conical island slopes. *Proc R Soc A* 472:20160052. <https://doi.org/10.1098/rspa.2016.0052>
- McFall BC, Fritz HM (2017) Runup of granular landslide generated tsunamis on planar coasts and conical islands. *J Geophys Res: Oceans* 122:6901–6922. <https://doi.org/10.1002/2017JC012832>
- McSaveney MJ (1978) Sherman Glacier rock avalanche, Alaska, U.S.A. In: Voight B (ed) *Rockslides and avalanches*, vol 14(A). Elsevier, Amsterdam, pp 197–258. <https://doi.org/10.1016/B978-0-444-41507-3.50014-3>
- Miller GS, Andy Take W, Mulligan RP, McDougall S (2017) Tsunamis generated by long and thin granular landslides in a large flume. *J Geophys Res Oceans* 122:653–668. <https://doi.org/10.1002/2016JC012177>
- Mohammed F (2010) Physical modeling of tsunamis generated by three-dimensional deformable granular landslides, PhD thesis, Ga. Inst of Tech, Atlanta
- Mohammed F, Fritz HM (2012) Physical modeling of tsunamis generated by three-dimensional deformable granular landslides. *J Geophys Res: Oceans* 117:C11015. <https://doi.org/10.1029/2011JC007850>
- Mohammed F, Fritz HM (2013) Correction to “Physical modeling of tsunamis generated by three-dimensional deformable granular landslides”. *J Geophys Res: Oceans* 118:3221. <https://doi.org/10.1002/jgrc.20218>
- Moore JG, Clague DA, Holcomb RT, Lipman PW, Normark WR, Torresan ME (1989) Prodigious submarine landslides on the Hawaiian ridge. *J Geophys Res: Sol Earth* 94:17465–17484
- Müller L (1964) The rock slide in the Vajont valley. *Rock Mech Eng Geol* 2(3–4):148–212
- Nonveiller E (1987) The Vajont reservoir slope failure. *Eng Geol* 24:493–512
- Ohmer M (1994) Schnelle und langsame Bewegungen mit der Pneumatik. *Pneumatic Tips* 39(86):25–29 (in German)
- Orteu JJ, Garric V, Devy M (1997) Camera calibration for 3D reconstruction: application to the measurement of 3D deformations on sheet metal parts. In *Lasers and Optics in Manufacturing III* (pp. 252–263). Intl Soc for Optics and Photonics
- Panizzo A, Girolamo PD and Petaccia A (2005) Forecasting impulse waves generated by subaerial landslides. *J Geophys Res* 110(C12)
- Plafker G, Ericksen GE (1979) Nevados Huascarán avalanches, Peru. *Rockslides and avalanches*. In: Voight B (ed) *Developments in geotechnical engineering 14A*, vol 1. Elsevier, Amsterdam, pp 277–314
- Plafker G, Erickson GE, Fernández Concha J (1971) Geological aspects of the May 31, 1970 Peru earthquake. *Bull Seismol Soc Am* 61(3):543–578
- Plüss C (1987) Experiments on granular avalanches. PhD thesis. Eidg. Tech. Hochschule, Zürich, Switzerland
- Poncet R, Campbell C, Dias F, Locat J, Mosher D (2010) A study of the tsunami effects of two landslides in the St. Lawrence estuary. Submarine mass movements and their consequences. *Adv Nat Technol Hazards Res* 28:755–764. https://doi.org/10.1007/978-90-481-3071-9_61
- Pudasani SP, Wang Y, Sheng L-T, Hsiao S-S, Hutter K, Katzenbach R (2008) Avalanching granular flows down curved and twisted channels: theoretical and experimental results. *Phys Fluids* 20(7):073302
- Raffel M, Willert CE, Kompenhans J (1998) *Particle image velocimetry—a practical guide*. Springer, Berlin
- Romano A, Di Risio M, Bellotti G, Molfetta MG, Damiani L, De Girolamo P (2016) Tsunami generated by landslides at the coast of conical islands: experimental benchmark dataset for mathematical model validation. *Landslides* 13:1379–1393. <https://doi.org/10.1007/s10346-016-0696-4>
- Roth GI, Mascenik DT, Katz J (1999) Measurements of the flow structure and turbulence within a ship bow wave. *Phys Fluids* 11:3512–3523
- Sartori M, Baillifard F, Jaboyedoff M, Rouiller JD (2003) Kinematics of the 1991 Randa rockslide (Valais, Switzerland). *Nat Hazards Earth Sys Sci* 3:423–433
- Savage SB, Hutter K (1989) The motion of granular material down a rough incline. *J Fluid Mech* 199:177–215
- Savage SB, Hutter K (1991) The dynamics of avalanches of granular materials from initiation to runout. Part I: Analysis *Acta Mech* 86:201–223
- Scarano F, Riethmuller ML (1999) Iterative multigrid approach in piv image processing with discrete window offset. *Exp Fluids* 26:513–523
- Scarano F, Riethmuller ML (2000) Advances in iterative multigrid piv image processing. *Exp Fluids* 29:S51–S60
- Scheidegger AE (1973) On the prediction of the reach and velocity of catastrophic landslides. *Rock Mech Rock Eng* 5:231–236. <https://doi.org/10.1007/BF01301796>
- Shreve RL (1966) Sherman landslide. *Alaska Sci* 154:1639–1643
- Shreve RL (1968) Leakage and fluidization in air-lubricated avalanches. *Geol Soc Am Bull* 79:653–658
- Synolakis CE, Bardet J, Borrero JC, Davies HL, Okal EA, Silver EA, Sweet S, Tappin DR (2002) Slump origin of the 1998 Papua New Guinea tsunami. *Proc R Soc A* 458:763–789
- Tai CY, Wang Y, Gray JMNT, Hutter K (1999) Methods of similitude in granular avalanche flows. In: Hutter K, Wang Y, Beer H (eds) *Advances in cold-regions thermal engineering and sciences*, lecture notes in physics, vol 533. Springer, Berlin, pp 415–428
- Tai YC, Gray JMNT, Hutter K (2001) Dense granular avalanches: mathematical description and experimental validation. In: Balmforth NL, Provenzale A (eds) *Geomorphological fluid mechanics*, lecture notes in physics, vol 582. Springer, Berlin, pp 339–366
- Tinti S, Manucci A, Pagnoni G, Armigliato A, Zaniboni R (2005) The 30 December 2002 landslide-induced tsunamis in Stromboli: sequence of the events reconstructed from the eyewitness accounts. *Nat Hazards Earth Sys Sci* 5:763–775
- Tinti S, Maramai A, Armigliato A, Graziani L, Manucci A, Pagnoni G, Zanoboni F (2006) Observations of physical effects from tsunamis of December 30, 2002 at Stromboli volcano, Southern Italy. *Bull Volcanol* 68:450–461
- Urgeles R, Locat J, Lee HJ, Martin F (2002) The Saguenay Fjord, Quebec, Canada: integrating marine geotechnical and geophysical data for spatial seismic slope stability and hazard assessment. *Mar Geol* 185:319–340

- Varnes DJ (1978) Slope movements type and processes, TRB, National Research Council, Washington, D.C, vol. 176 of Landslides analysis and control, 11–33
- Voight B, Glicken H, Janda R, Douglass P (1981) Catastrophic rockslide avalanche of may 18. In: Lipman PW, Mullineaux DR (eds) The 1980 eruptions of Mount St. Helens, vol 1250. U.S. Geological Survey Professional Paper, Washington, DC, pp 347–378
- Voight B, Janda R, Douglass P (1983) Nature and mechanics of the Mount St. Helens rockslide-avalanche of 18 May 1980. *Geotechnique* 33:243–273
- Walder JS, Watts P, Sorensen OE, Janssen K (2003) Tsunamis generated by subaerial mass flows. *J Geophys Res* 108(B5):2236
- Watts P (2000) Tsunami features of solid block underwater landslides. *J Waterw Port Coast Ocean Eng* 126(3):144–152
- Weiss R, Fritz HM, Wünnemann K (2009) Hybrid modeling of the megatsunami runup in Lituya Bay after half a century. *Geophys Res Lett* 36:L09602
- Westerweel J (2000) Theoretical analysis of the measurement precision in particle image velocimetry. *Exp Fluids* 29:53–512
- Westerweel J, Dabiri D, Gharib M (1997) The effect of a discrete window offset on the accuracy of cross-correlation analysis of digital piv recordings. *Exp Fluids* 23:20–28
- Wieland M, Gray JMNT, Hutter K (1999) Channelized free surface flow of cohesionless granular avalanche in a chute with shallow lateral curvature. *J Fluid Mech* 293:73–100
- Xenakis AM, Lind SJ, Stansby PK, Rogers BD (2017) Landslides and tsunamis predicted by incompressible smoothed particle hydrodynamics (SPH) with application to the 1958 Lituya Bay event and idealized experiment. *Proc R Soc A* 473(2199):20160674. <https://doi.org/10.1098/rspa.2016.0674>
- Yavari-Ramshe S, Ataie-Ashtiani B (2017) A rigorous finite volume model to simulate subaerial and submarine landslide-generated waves. *Landslides* 14:203–222. <https://doi.org/10.1007/s10346-015-0662-6>
- Zweifel A, Hager WH, Minor H-E (2006) Plane impulse waves in reservoirs. *J Waterw Port Coast Ocean Eng* 132:358–368. [https://doi.org/10.1061/\(ASCE\)0733-950X\(2006\)132:5\(358\)](https://doi.org/10.1061/(ASCE)0733-950X(2006)132:5(358))

B. C. McFall (✉)

U.S. Army Engineer Research and Development Center,
3909 Halls Ferry Road, Vicksburg, MS 39180, USA
Email: brian.c.mcfall@usace.army.mil

B. C. McFall · F. Mohammed · H. M. Fritz · Y. Liu

School of Civil and Environmental Engineering,
Georgia Institute of Technology,
Atlanta, GA 30332, USA

F. Mohammed

e-mail: fahad.mohammed@fmglobal.com

H. M. Fritz

e-mail: fritz@gatech.edu

Y. Liu

e-mail: yibinliu@gatech.edu

F. Mohammed

Research Division,
Center for Property Risk Solutions, FM Global,
1151 Boston-Providence Tpke, Norwood, MA, USA